ACS APPLIED MATERIALS & INTERFACES

Research Article

Cite This: ACS Appl. Mater. Interfaces 2019, 11, 24164−24171

www.acsami.org

Low-Temperature Catalytic Graphitization to Enhance Na-Ion Transportation in Carbon Electrodes

Yiwei Li,[†] Jiangtao Hu,[†] Ziqi Wang,[†] Kai Yang,[†] Weiyuan Huang,[†] Bo Cao,[†] Zhibo Li,[†] Wei Zhang,*[,‡] and Feng Pan*[,†]

[†]School of Advanced Materials, Peking University Shenzhen Graduate School, Shenzhen 518055, People's Republic of China

[‡]Sustainable Energy Technologies Department, Brookhaven National Laboratory, Upton, New York 11973, United States

Supporting Information

ABSTRACT: Sodium-ion batteries (SIBs) are now emerging as a low-cost alternative to the current lithium-ion batteries, but their performance is limited by the sluggish transportation of large Na ions in electrodes. Expanded graphite has been employed in enhancing the transport kinetics. However, high-performance graphite should be synthesized at high temperatures when using traditional methods, which inevitably increases the total cost of material production. To tackle the kinetic issue for SIBs, we develop a three-dimensional network of graphene during catalytic graphitization in carbon electrodes at a temperature as low as 450 °C by using Prussian blue as a precursor. Furthermore, a strategy is proposed to enhance the transport ability of the Na-ion in the network by controlling the diffusion distance of the Fe cluster and the distance between Prussian blue particles, leading to optimized performance with both excellent high-rate performance (167 mAh g^{-1} at 1.0 A g^{-1}) and high charging capacity (390 mAh g^{-1} at 0.05 A g^{-1}). The results provide insights into the engineering of ionic transport properties through low-temperature catalytic graphitization in electrodes for SIBs and help design high-performance and low-cost electrodes for large-scale energy storage systems.

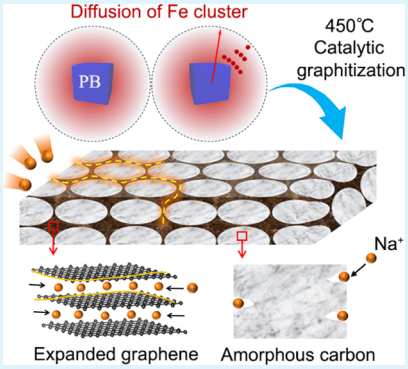

KEYWORDS: *sodium-ion battery, catalytic graphitization, Prussian blue, graphene, ionic transport*

INTRODUCTION

The development of cost-effective energy storage systems with superior performance is critical to their large-scale applications in transportation vehicles, electrical grid, wind, and solar power systems.[1] Although lithium-ion batteries (LIBs) have become the predominant energy system for a wide range of applications, they are still costly, and the limited supply of lithium resources may become a major issue for the future of manufacturing industry.[2] In contrast, sodium-ion batteries (SIBs) have the advantage of lowering the manufacturing cost because sodium is abundantly available in nature.[3] However, because the ionic radius of a sodium ion (1.02 Å) is larger than that of a lithium ion (0.67 Å), it is difficult to accommodate sodium ions in the electrodes commonly used in LIBs.[4,5] As a consequence, many kinds of electrodes have been developed to be suitable for Na-ion storage in SIBs, such as carbon-based materials, titanium-based oxides, transitionmetal oxide, and alloy-based materials.[6−8] Among all the electrodes, amorphous carbon (AC) is one of the most promising candidates for large-scale SIBs, owing to its low cost, high electrochemical activity, high capacity, and safety,[9−12] which are crucial characters related to the practical applications of SIBs.

Despite their advantages, the AC electrodes still suffer from a kinetic issue associated with relatively low electronic conductivity (~1 × 10^2 S cm^{-1}) and sluggish mobility of Na ions (~10^{-9} cm^2 s^{-1}) that is originated from its intrinsic disordered structure.[9,13,14] The disordered structure will cause difficulty in transportation of Na ions owing to its different orientations and difficulty in transport of electronics owing to the amount of sp^3 hybrid orbitals between two carbon atoms, thus resulting in insufficient rate capability. Such a kinetic problem is also a major obstacle to the development of other types of electrodes for SIBs.[15] Several effective strategies have been applied to enhance the kinetics of electron/Na-ion transfer, such as designing porous structures for rapid Na-ion diffusion over a short distance[16,17] and introducing a graphene component with superb electronic conductivity (10^3 S/m).[13,18] One drawback of graphene is its small interlayer distance (~0.34 nm) that impedes Na-ion intercalation, but recently Na-ion storage in graphene can be enabled by using the ether-based electrolyte, such as diethylene glycol dimethyl ether (DEGDME).[19−21] It is attributed to the fast movement of the [Na−DEGDME]$^+$ complex between the layers, thus causing a high diffusivity of Na ions (1.1 × 10^{-8} cm^2 s^{-1}) in graphite.[22] The kinetics of Na-ion transport can be further improved by expanding graphene to possess an enlarged interlayer distance

Received: April 24, 2019
Accepted: June 19, 2019
Published: June 19, 2019

DOI: 10.1021/acsami.9b07206
ACS Appl. Mater. Interfaces 2019, 11, 24164−24171

(>0.37 nm),[23,24] and the expanded graphene (EG) has been generated by reducing the number of stacking layers.[25] Unfortunately, in order to obtain high-quality graphene embedded within the AC matrix, most AC materials have to be graphitized at high temperatures (>1400 °C),[26−29] which undoubtedly increases the total energy cost for fabricating SIBs.

To develop cost-effective synthetic technologies without sacrificing the performance of graphene/AC composites,[30] catalytic graphitization using transition-metal catalysts, such as Fe, Ni, and Co, has become attractive due to the synthesis at temperatures as low as 500 °C,[31−33] which has been widely applied in producing various materials such as electrocatalysts,[34] electrodes for capacitors and batteries,[31,35] and monolayer graphene.[36] The catalytic temperature and quality of graphene strongly depend on the precursors. By choosing a precursor of Prussian blue (PB), most studies have disclosed a simple, low-cost, and efficient synthetic route to prepare high-quality graphene.[37−41] The use of PB as a novel precursor for catalytic graphitization has three important advantages: (a) it contains Fe that is one of the most effective catalysts to lower the synthesis temperature;[31,33] (b) it is a soft template that enables the synthesis of highly ordered graphene;[40] (c) it can be converted to a nanoporous carbonaceous structure that enhances the Na-ion mobility in anode electrodes for SIBs.[39] Therefore, our previous work has used PB to successfully transform AC to high-performance graphene at 650 °C,[38,41] but we are also aware that the catalytic temperature can be further reduced for a low-cost synthetic process. Equally importantly, to maximize the Na-ion transportation of carbon composites relies on how to regulate the distribution of graphene within porous carbon electrodes.[9,18] However, the mechanisms underlying the structural design and engineering while using PB for catalytic graphitization remain unclear.

Herein, we synthesized high-performance hybrid materials of graphene/AC composites (G-AC) at the lowest temperature (450 °C) reported so far, by using PB particles as a precursor to generate various sizes of Fe nanoparticles during catalytic graphitization, which ensured the availability of a three-dimensional network containing interconnected carbonaceous nanopores and graphene with various structures. The mechanisms of engineering the hybrid architecture were identified. Specifically, the structure and interlayer distance of graphene can be modified through adjusting the diffusion distance of the Fe cluster within the AC matrix and the space between PB particles, which is key to maximizing the transport ability of the electron/Na-ion in the three-dimensional network. Therefore, the electrochemical performance of graphite/AC electrodes was optimized to achieve excellent rate performance (167 mAh g^{-1} at 1000 mA g^{-1}), high charging capacity in the first cycle (390 mAh g^{-1} at 50 mA g^{-1}), and superb Coulombic efficiency (100% retention over 100 cycles).

EXPERIMENTAL SECTION

Synthesis of G-AC-*n*. PB (purchased from Adamas-beta) and glucose (purchased from sinoreagent) were mixed in different proportions, and the mass ratios between PB and glucose were 10:1, 10:2, 10:3, 10:4, and 10:5 for G-AC-1 to G-AC-5, which means the mass fraction of PB was 90.91, 83.33, 76.92, 71.43, and 66.67%, respectively. These two materials were mixed with water and ethanol and grinded over 30 min in an agate mortar. Then, the mixture was dried at 80 °C in air, followed by annealing at 450 °C for 6 h in Ar/H_2 (95:5). After that, when the calcined product was exposed to air, the reduction product of Fe nanoparticles would react with oxygen, causing a combustion phenomenon (spark while stirring) during the oxidization process. The combustion product was washed by H_2SO_4 solution for 8 h, and then filtered with water and dried at 80 °C in a vacuum oven. The final products were named as G-AC-1, G-AC-2, G-AC-3, G-AC-4, and G-AC-5 according to the original mass ratio.

Structural Characterization. X-ray diffraction (XRD, Bruker D8 ADVANCE diffractometer with Cu Kα, λ = 1.5405 Å) was used to analyze the crystal structure of the samples. The graphitization degree of the five materials was detected by the microlaser confocal Raman spectrometer (HORIBA LabRAM HR800). The scanning electron microscope (SEM, Zeiss Supra 55 field emission scanning electron microscopy) and transmission electron microscope (TEM, FEI Tecnai G2 F30) were used to observe the morphologies at the electrode scale and the structures of the samples at the atomic scale, respectively. The adsorption and specific surface area tester (Micromeritics ASAP 2020 HD88) were used to obtain the specific surface areas of the samples by the nitrogen adsorption−desorption method, and the pore size distribution was derived from the adsorption isotherm according to the Barrett−Joyner−Halenda model.

Electrochemical Testing. Coin cells were assembled in a glovebox filled with argon. The active material G-AC-*n*, acetylene black, and polyvinylidene fluoride were poured into *N*-methyl pyrrolidone with a weight ratio of 7:2:1. To obtain the working electrode, the final slurry was then spread on Cu foil and dried at 120 °C in a vacuum oven. Pure sodium and glass fiber (Whatman GF/A) were chosen as a counter electrode and a separator, respectively. The electrolyte was 1 M sodium trifluomethanesulfonate ($NaCF_3SO_3$) in DEGDME. The cyclic and rate performance was tested by the NEWARE system between 0.01 and 3.0 V. Cyclic voltammetry (CV) data were collected by the electrochemistry workstation (CHI604E).

RESULTS AND DISCUSSION

Figure 1a illustrates the process to synthesize the G-AC composites via metal-catalytic graphitization at a low temperature of 450 °C (see details in the Experimental Section). The catalytic temperature of 450 °C is the lowest one for graphitization because this is the lowest temperature for complete decomposition of the precursor (Figure S1). First of all, by tuning the mass of glucose, all PB particles were designed to embed within glucose, which is critical for establishing a three-dimensional nanoporous structure. The PB particles possess an average size of about 80.5 nm (Figure 1b). The precursor was calcined at 450 °C in an Ar/H_2 atmosphere, during which glucose was converted to AC (step i).[42] Meanwhile, the Fe cluster was gradually released from PB and diffused into the AC matrix. According to Fick's second law,[43] the concentration of the Fe cluster should decrease with increasing distance from PB. After the Fe cluster diffused out of PB particles, the cyanide groups released from the PB structure in the gaseous form, leaving behind a nanoporous carbonaceous architecture.[44] During step ii, the Fe cluster in the AC matrix would agglomerate to form metallic Fe nanoparticles. Owing to different concentrations of the Fe cluster, various Fe nanoparticles could possess different sizes. Here, we should note that Fe nanoparticles would not be directly formed at the positions of PB particles during the decomposition of PB, as discussed in Note S1. According to the phase diagram of the Fe−C system, the Fe ions on the surface would react with AC to form iron carbides at 450 °C.[38,45] During step iii, because the iron carbides are metastable phases in the Fe−C system,[45] catalytic graphitization took place through the decomposition of iron carbides into Fe nanoparticles and graphene.[33] During step iv, Fe nanoparticles were oxidized to be Fe_2O_3 when they were

DOI: 10.1021/acsami.9b07206
ACS Appl. Mater. Interfaces 2019, 11, 24164−24171

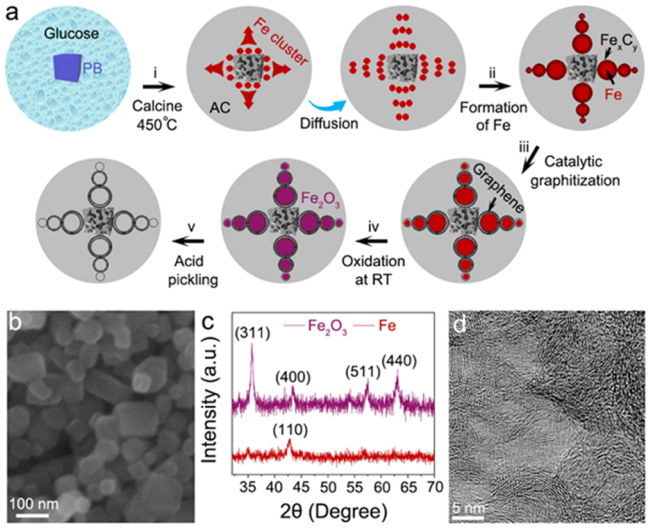

Figure 1. Synthesis of graphene/AC (G-AC) composites via metal-catalytic graphitization at 450 °C (a) schematic illustration of the synthetic process. Catalytic graphitization took place through the decomposition of iron carbides Fe_xC_y in step iii. In the final products, a three-dimensional network containing interconnected graphene and carbonaceous nanopores was formed within the AC matrix. (b) SEM image of PB particles with an average size of about 80.5 nm. (c) XRD patterns of the intermediate products, demonstrating the formation of Fe before oxidation (step iv), which was converted to Fe_2O_3 after oxidation. (d) TEM image of final products, showing the morphology of interconnected graphite.

exposed to air at room temperature. It can be supported by the XRD patterns of the intermediate products before (the products were obtained before oxidized through mixed with water to inhibit the products exposed to oxygen) and after oxidation, in which a (110) peak of metallic Fe was observed before oxidation, and then it was absent, accompanied by emergence of diffraction peaks of Fe_2O_3 after oxidation (Figure 1c). Finally, Fe_2O_3 nanoparticles were dissolved by acid, leaving behind the spherical graphene embedded within the matrix of the AC electrode, as shown in Figure 1d. The graphene interconnected with each other and linked the carbonaceous nanopores to form a three-dimensional network, which guarantees fast electron/Na^+ transport within the AC matrix.

The structure of graphene in the composites is tunable by changing the mass fraction of PB in the precursor (Figure 2a,b). When the mass fraction of PB was 90.91% (G-AC-1), a $(002)_G$ peak was observed at 26.6° in the XRD pattern, corresponding to the normal graphene with an interlayer distance of 0.335 nm (Figure 2b). After decreasing the mass fraction of PB to 83.33% (G-AC-2), an extra and broad peak was detected at a lower angle of 26.3°, owing to the formation of EG with an enlarged interlayer distance of 0.338 nm. When the mass fraction of PB gradually decreased, the $(002)_{EG}$ peak continuously shifted to the left, indicating the increasing interlayer distance of EG (Figure 2b). Interestingly, only one $(002)_{EG}$ peak was visible in the XRD pattern of G-AC-4 (Figure 2a), suggesting that EG is the dominant component of graphene in this sample. Raman spectroscopy was applied to evaluate the degree of graphitization, by using the intensity ratio between the crystalline graphene band G and the disordered carbon band D (I_G/I_D) (Figure S2 and Note S2).[46] The value decreased when the mass fraction of PB decreased,

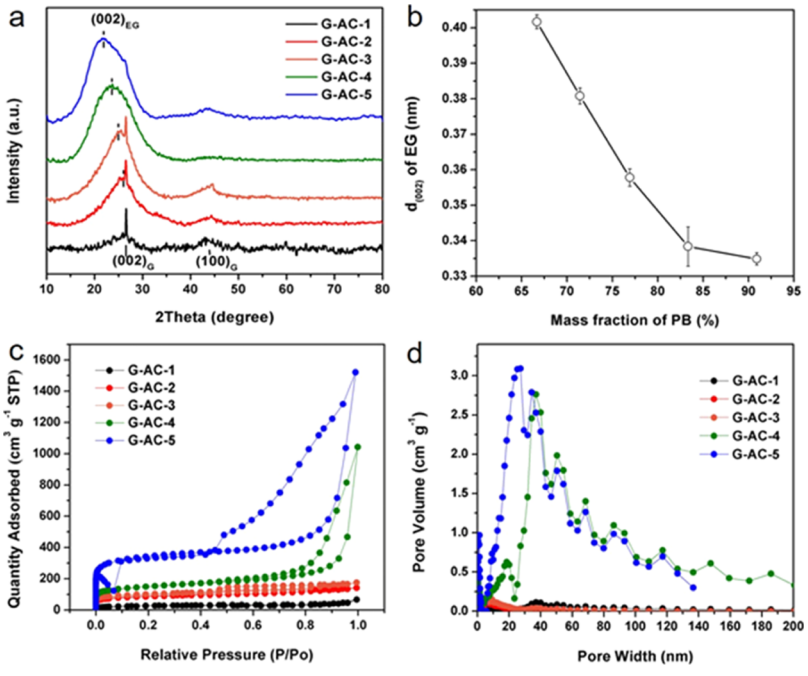

Figure 2. Tunable structure of G-AC composites while changing the mass fraction of PB. (a) XRD patterns of G-AC-1 to G-AC-5. Only diffraction peaks of normal graphene (marked by solid black lines) were observed in G-AC-1, but a broad peak of EG (marked by dashed lines) emerged and shifted to the left from G-AC-2 to G-AC-5. (b) Evolution of interlayer distance $d_{(002)}$ of EG as a function of mass fraction of PB. The values of $d_{(002)}$ were obtained from fitting of the peak position in (a) using a Gaussian function. The mass fraction of PB was 90.91% for G-AC-1, 83.33% for G-AC-2, 76.92% for G-AC-3, 71.43% for G-AC-4, and 66.67% for G-AC-5. (c) Nitrogen adsorption−desorption isotherms of G-AC-1 to G-AC-5, showing the increasing specific surface area of the composites with the decrease of mass fraction of PB. (d) Pore size distribution of G-AC-1 to G-AC-5, showing a significant increase of pore volume in G-AC-4 and G-AC-5.

DOI: 10.1021/acsami.9b07206
ACS Appl. Mater. Interfaces 2019, 11, 24164−24171

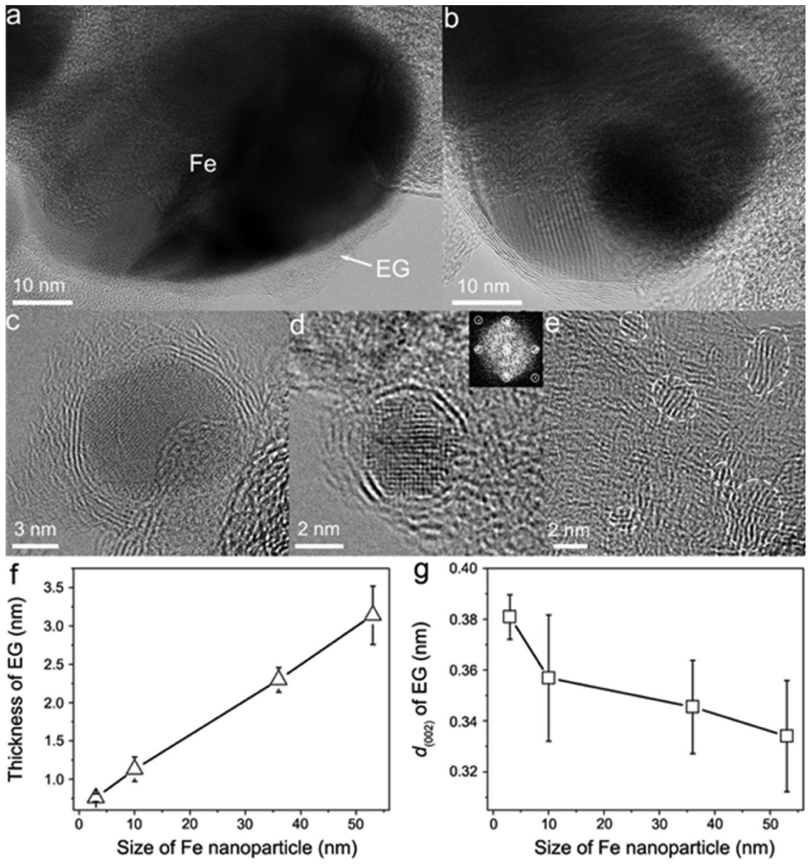

Figure 3. Structure of Fe nanoparticles coated by EG in G-AC composites. (a–e) HRTEM images of Fe nanoparticles in G-AC-1 to G-AC-5, respectively. The inset in (d) is the FFT pattern corresponding to the Fe nanoparticle in (d). The dashed circles in (e) mark the location of graphene domains in G-AC-5. (f–g) Evolution of thickness of EG and interlayer distance $d_{(002)}$ of EG as a function of the size of Fe nanoparticles, respectively. All the values were extracted from the HRTEM images in (a–d).

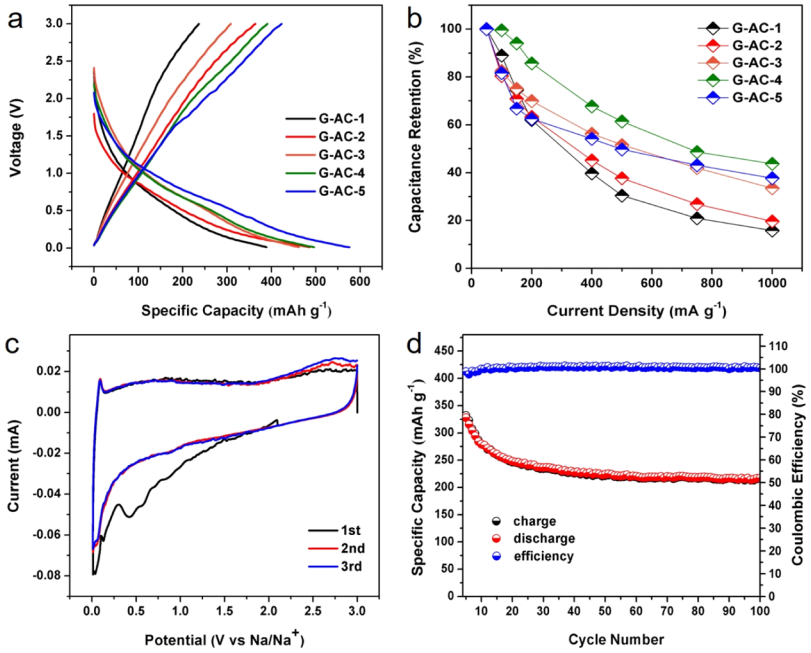

Figure 4. Electrochemical performance of the G-AC composites in SIBs. (a) Charge–discharge profiles at 50 mA g^{-1} for the first cycle. (b) Capacity retention at different current densities. (c) CV curves of G-AC-4 at 0.1 mV s^{-1} with a voltage window between 0.01 and 3.0 V. (d) Cycling performance and Coulombic efficiency of G-AC-4 at 0.5 A g^{-1} for 100 cycles.

revealing a progressive decrease of graphitization. The high-resolution X-ray photoelectron spectroscopy (XPS) results of C 1s could be divided into five parts as shown in Figure S3, and the proportion of C═C and C–C were calculated and

DOI: 10.1021/acsami.9b07206
ACS Appl. Mater. Interfaces 2019, 11, 24164–24171

shown in Table S1. The percentage of C=C decreases from G-AC-1 to G-AC-5, indicating that a reduced degree of graphitization, which well corresponds to the results of Raman and XRD data. The nitrogen adsorption−desorption isotherm in Figure 2c shows that the specific surface area of the composites increased with the decrease of mass fraction of PB, that is, 95 $m^2 g^{-1}$ for G-AC-1, 298.3 $m^2 g^{-1}$ for G-AC-2, 346.8 $m^2 g^{-1}$ for G-AC-3, 522.1 $m^2 g^{-1}$ for G-AC-4, and 1182.5 $m^2 g^{-1}$ for G-AC-5. The large surface area of AC provides abundant sites, such as defects, for efficient Na-ion storage.[47] Furthermore, the pore size distribution of various G-AC samples shows the existence of nanopores in all the samples but a significant increase of pore volume in G-AC-4 and G-AC-5, which facilitates the fast transport of Na ions in these two composites (Figure 2d).

Intrigued by the variable interlayer distance of EG as a function of the mass fraction of PB, high-resolution TEM (HRTEM) imaging was performed on graphene-coated Fe nanoparticles so as to reveal the factors dominating the regulation of the graphene structure (Figure 3). The Fe nanoparticles were preserved before oxidation at room temperature. The Fe nanoparticles were thoroughly coated by long-range-ordered stacking layers of EG in samples of G-AC-1 to G-AC-4 (Figure 3a−d). The fast Fourier transform (FFT) pattern in Figure 3d shows that Fe nanoparticles have the body-centered cubic structure. In contrast, some graphene domains with short-range ordering were detected in a localized region of G-AC-5, in which no Fe nanoparticle is visible (Figure 3e). A close TEM examination revealed that the thickness of EG increased with the increase of the size of the Fe nanoparticle (Figure 3f). The change of the particle size is also linked to the evolution of the average interlayer distance of EG that was measured through the line scan analysis across the stacking layers in Figure 3a−d, showing the decreasing interlayer distance with the increase of particle size (Figure 3g). According to the values of interlayer distance and thickness of EG, the average numbers of stacking layers can be estimated to be 11, 7, 3, and 2 in Figure 3a−d, respectively. It implies that the reduction in the interlayer distance may result from the increase of the stacking layers of EG, which is similar to the results obtained in graphene nanosheet materials.[25] In a word, the larger size of the Fe nanoparticle leads to the smaller interlayer distance and more stacking layers, implying the possibility of tuning the structures of EG by controlling the size of the Fe nanoparticle.

Changing the mass fraction of PB not only adjusts the structures of G-AC composites but also optimizes the performance to achieve both high capacity and excellent high-rate capability (Figure 4). The electrochemical performances of AC derived from glucose at 450 °C are shown in Figure S4. However, the AC derived from glucose exhibits only ∼70 mA h g^{-1}, which illustrates the importance of PB decomposition catalysis. Figure 4a shows the discharge/charge profiles of all the samples in the first cycle under a current density of 50 mA g^{-1}, demonstrating an increasing specific capacity from G-AC-1 to G-AC-5. The G-AC-5 electrode delivered a maximum charging capacity of 420 mA h g^{-1}, owing to the largest surface area in all samples. However, such a high-capacity electrode has serious capacity degradation at low current densities (Figure 4b), which delivered 157 mA h g^{-1} at 1000 mA g^{-1} that only recovered to 268 mA h g^{-1} after reducing the current density to 50 mA g^{-1} (Figure S5). The quick capacity degradation could be attributed to the poor electronic conductivity of G-AC-5, which has not formed any effective conductive network. In contrast, the G-AC-4 electrode, which displays the second-highest charging capacity of 390 mA h g^{-1} at 50 mA g^{-1}, possesses the best rate performance of 167 mA h g^{-1} at 1000 mA g^{-1} that can recover to 372 mA h g^{-1} while the current density returned to 50 mA g^{-1} (Figure S5). Therefore, only the G-AC-4 composite possesses the optimized electrochemical properties with high capacity and excellent high-rate capability. The CV curves of G-AC-4 for the first three cycles are shown in Figure 4c. There is a pair of oxidation−reduction peaks at around 0.1 V, corresponding to the insertion and extraction of sodium ions in graphite. No significant peak was observed when the voltage was larger than 0.1 V, indicating the existence of capacitance behavior resulting from the large specific surface area. In addition, the peak at around 0.5 V, which was present in the first cycle, disappeared in the subsequent cycles, representing the formation of the SEI layer.[48] Figure 4d displays the cycle performance of G-AC-4. A quick capacity degradation occurred at the first ten circles due to the interface activation and reconstruction, which consumed sodium ions and caused irreversible capacity loss. While the interface is stable, it can maintain a high capacity of 201 mA h g^{-1} at a current density of 500 mA g^{-1} after 100 cycles, and the Coulombic efficiency was maintained to be 100% after 100 cycles. Such stable electrochemical performance is better than most carbon materials reported so far (Table S2).

The multifaceted analysis of various hybrid G-AC materials enlightened us the mechanisms underlying the architectural regulation and the related electrochemical performance. In order to form tiny Fe nanoparticles, the diffusion of the Fe cluster should occur during catalytic graphitization, as discussed in Note S1. Because the precursor was calcined at 450 °C for a limited duration (step i), the Fe cluster can only be allowed to diffuse a certain distance (called diffusion radius R_{diff} henceforth), as illustrated in Figure 5a. Here, the diffusion model is simplified as spherical geometry, and R_{diff} is defined as the distance between the location of Fe cluster sources (PB particles) and the point of the Fe cluster disappearance due to the concentration decay (Figure 5a). In the following text, we simply assume that each PB particle contains the same number of Fe ions. Therefore, given that the calcination temperature and duration kept the same for all samples, R_{diff} and the concentration gradient of the Fe cluster along the radial direction were assumed to be identical for each sphere model. When the distance between two PB particles d_{PB} is larger than $2R_{diff}$, the higher concentration of the Fe cluster in the inner regions closer to PB particles, the more Fe clusters can aggregate into larger spherical Fe nanoparticles, and therefore, that trigger the formation of spherical graphene (Figure 5b). In contrast, the amount of Fe clusters in the outer region of the sphere model is too low to efficiently create spherical Fe nanoparticles, leading to the formation of graphene domains (Figure 5b), as evidenced by the HRTEM image of G-AC-5 in Figure 3e. Once the mass fraction of PB is increased to make d_{PB} equal to $2R_{diff}$, two sphere models are connected thus doubling the Fe cluster concentration in the outer region (Figure 5c). Therefore, tiny and spherical Fe nanoparticles are formed, coated by EG with a large interlayer distance, as evidenced by the HRTEM image of G-AC-4 (Figure 3d). With further increase of PB concentration from G-AC-3 to G-AC-1, d_{PB} gradually decreases to be lower than $2R_{diff}$, forcing more and more Fe clusters to aggregate into larger Fe nanoparticles

DOI: 10.1021/acsami.9b07206
ACS Appl. Mater. Interfaces 2019, 11, 24164−24171

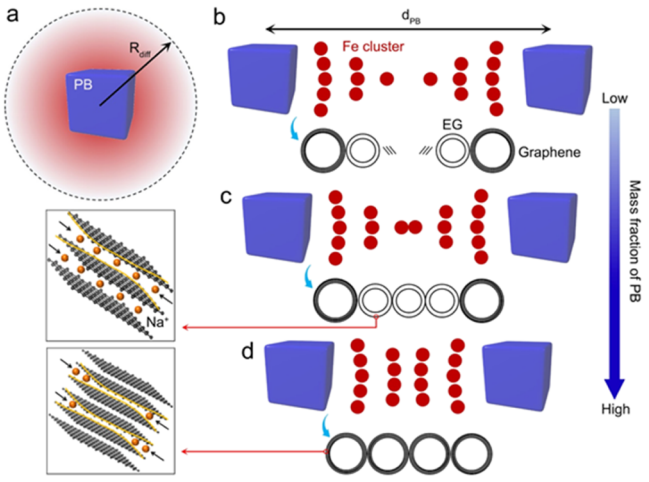

Figure 5. Schematic illustration of structural evolution via changing the mass fraction of PB. (a) Spherical diffusion model showing the diffusion of the Fe cluster (red color) out of the PB particles. The R_{diff} is the distance between the location of PB particles and the point of the Fe cluster disappearance due to the concentration decay (marked by a dashed circle). (b–d) Structural change of graphene while increasing the mass fraction of PB. When d_{PB} is larger than $2R_{diff}$ in (b), graphene domains (marked by straight lines) are formed in the outer region of the sphere model. When d_{PB} is equal to $2R_{diff}$ in (c), EG with large interlayer distance becomes the dominant component of graphene. Further reduction of d_{PB} will diminish the amount of EG in (d). In contrast to the sluggish Na-ion diffusion in normal graphene due to the small interlayer distance, the existence of EG facilitates the transport of Na ions (marked by brown dots) in EG.

wrapped by EG with decreased interlayer distance (Figure 5d). In all the samples except G-AC-5, the spherical EG connect to each other, forming a three-dimensional network for fast electron/Na-ion diffusion in the AC matrix.

With the underpinning knowledge concerning the structural evolution as a function of the ratio of d_{PB} to R_{diff}, it provides guidance for designing the G-AC architectures with optimized high-rate capability. Because the nanopore structure of G-AC-4 is similar to that of G-AC-5 (Figure 2d), it would provide a similar contribution to Na-ion transport in these two samples. Therefore, the difference of Na-ion transport and its induced high-rate capability in G-AC-4 and G-AC-5 mainly results from different structures of EG. When decreasing the mass fraction of PB, more and more Fe nanoparticles with small sizes are formed (Figure 5), leading to an increase of interlayer distance of EG (Figure 3g). The larger the interlayer distance is, the faster the EG accommodates Na ions.[23] Therefore, the high-rate performance gradually increased from G-AC-1 to G-AC-4 (Figures 4b and S5). It is maximized when the value of d_{PB}/R_{diff} is optimized to be 2. However, after further increasing the value of d_{PB}/R_{diff} in G-AC-5, the spherical EG disconnect to each other in the outer region of the sphere model (Figure 5b), owing to the formation of randomly distributed graphene domains. Consequently, it causes the breakdown of the three-dimensional network; thus, the fast Na-ion diffusion is interrupted, leading to the degradation of high-rate capability in G-AC-5.

CONCLUSIONS

In summary, we demonstrated that establishing a three-dimensional network of EG within the AC matrix promised great potential for improving the kinetics of Na-ion transport in electrodes for SIBs. A cost-effective synthetic route was introduced to convert the AC material to high-quality EG through catalytic graphitization at the lowest temperature of 450 °C reported so far. The use of PB particles as the precursor enabled the adjustment of the graphene structure that facilitates Na-ion diffusion within the AC electrode. For the first time, the results elucidated the mechanism governing the structural evolution of graphene during catalytic graphitization. It guided us to maximize the transport ability of electron/Na ion in the three-dimensional network by controlling the diffusion distance of Fe clusters within the AC matrix that released from PB particles and the distance between PB particles that is tunable by changing the mass fraction of PB. Therefore, the performance of graphene/AC electrodes was optimized to deliver excellent high-rate performance (167 mAh g^{-1} at 1000 mA g^{-1}), a high initial charging capacity (390 mAh g^{-1} at 50 mA g^{-1}), superb Coulombic efficiency (100% retention over 100 cycles), and acceptable cycling stability (about 60.4% capacity maintained after 100 cycles at 500 mA g^{-1}). Our work opened a new avenue for designing novel architectures in carbon electrodes with the desired performance. Furthermore, with the underpinning knowledge, new strategies in structural engineering of electrodes and optimization of electrochemical properties can be developed for fabricating low-cost and high-performance batteries for large-scale applications.

ASSOCIATED CONTENT

Supporting Information

The Supporting Information is available free of charge on the ACS Publications website at DOI: 10.1021/acsami.9b07206.

Detailed introduction of XRD, details of Raman data, XPS, rate performance, and electrochemical performance, and difference analysis (PDF)

AUTHOR INFORMATION

Corresponding Authors

*E-mail: zhangw@bnl.gov (W.Z.).
*E-mail: panfeng@pkusz.edu.cn (F.P.).

ORCID

Feng Pan: 0000-0002-8216-1339

Notes

The authors declare no competing financial interest.

ACKNOWLEDGMENTS

This work was financially supported by National Materials Genome Project (2016YFB0700600), the National Natural Science Foundation of China (nos. 21603007 and 51672012), and Shen-zhen Science and Technology Research Grant (nos. JCYJ20150729111733470 and JCYJ20151015162256516).

REFERENCES

(1) Liu, J.; Zhang, J.-G.; Yang, Z.; Lemmon, J. P.; Imhoff, C.; Graff, G. L.; Li, L.; Hu, J.; Wang, C.; Xiao, J.; Xia, G.; Viswanathan, V. V.; Baskaran, S.; Sprenkle, V.; Li, X.; Shao, Y.; Schwenzer, B. Materials science and materials chemistry for large scale electrochemical energy storage: from transportation to electrical grid. *Adv. Funct. Mater.* **2013**, *23*, 929–946.

(2) Tarascon, J.-M. Is lithium the new gold? *Nat. Chem.* **2010**, *2*, 510.

(3) Slater, M. D.; Kim, D.; Lee, E. Sodium-Ion Batteries. *Adv. Funct. Mater.* **2013**, *23*, 947–958.

DOI: 10.1021/acsami.9b07206
ACS Appl. Mater. Interfaces 2019, 11, 24164–24171

(4) Johnson, V. L.; Ceder, G. Challenges for Na-ion negative electrodes. *J. Electrochem. Soc.* **2011**, *158*, A1011−A1014.
(5) Xu, Y.; Zhu, Y.; Liu, Y.; Wang, C. Electrochemical performance of porous carbon/tin composite anodes for sodium-ion and lithium-ion batteries. *Adv. Energy Mater.* **2013**, *3*, 128−133.
(6) Kim, S.-W.; Seo, D.-H.; Ma, X.; Ceder, G.; Kang, K. Electrode Materials for Rechargeable Sodium-Ion Batteries: Potential Alternatives to Current Lithium-Ion Batteries. *Adv. Energy Mater.* **2012**, *2*, 710−721.
(7) Wang, L. P.; Yu, L.; Wang, X.; Srinivasan, M.; Xu, Z. J. Recent developments in electrode materials for sodium-ion batteries. *J. Mater. Chem. A* **2015**, *3*, 9353−9378.
(8) Yabuuchi, N.; Kubota, K.; Dahbi, M.; Komaba, S. Research development on sodium-ion batteries. *Chem. Rev.* **2014**, *114*, 11636−11682.
(9) Balogun, M.-S.; Luo, Y.; Qiu, W.; Liu, P.; Tong, Y. A review of carbon materials and their composites with alloy metals for sodium ion battery anodes. *Carbon* **2016**, *98*, 162−178.
(10) Hou, H.; Qiu, X.; Wei, W.; Zhang, Y.; Ji, X. Carbon Anode Materials for Advanced Sodium-Ion Batteries. *Adv. Energy Mater.* **2017**, *7*, 1602898.
(11) Irisarri, E.; Ponrouch, A.; Palacin, M. R. Review-Hard Carbon Negative Electrode Materials for Sodium-Ion Batteries. *J. Electrochem. Soc.* **2015**, *162*, A2476−A2482.
(12) Stevens, D. A.; Dahn, J. R. High Capacity Anode Materials for Rechargeable Sodium-Ion Batteries. *J. Electrochem. Soc.* **2000**, *147*, 1271−1273.
(13) Marinho, B.; Ghislandi, M.; Tkalya, E.; Koning, C. E.; de With, G. Electrical conductivity of compacts of graphene, multi-wall carbon nanotubes, carbon black, and graphite powder. *Powder Technol.* **2012**, *221*, 351−358.
(14) Park, M.; Zhang, X.; Chung, M.; Less, G. B.; Sastry, A. M. A review of conduction phenomena in Li-ion batteries. *J. Power Sources* **2010**, *195*, 7904−7929.
(15) Dai, Z.; Mani, U.; Tan, H. T.; Yan, Q. Advanced Cathode Materials for Sodium-Ion Batteries: What Determines Our Choices? *Small Methods* **2017**, *1*, 1700098.
(16) Wenzel, S.; Hara, T.; Janek, J.; Adelhelm, P. Room-temperature sodium-ion batteries: Improving the rate capability of carbon anode materials by templating strategies. *Energy Environ. Sci.* **2011**, *4*, 3342−3345.
(17) Tang, K.; Fu, L.; White, R. J.; Yu, L.; Titirici, M.-M.; Antonietti, M.; Maier, J. Hollow Carbon Nanospheres with Superior Rate Capability for Sodium-Based Batteries. *Adv. Energy Mater.* **2012**, *2*, 873−877.
(18) Yan, Y.; Yin, Y.-X.; Guo, Y.-G.; Wan, L.-J. A Sandwich-Like Hierarchically Porous Carbon/Graphene Composite as a High-Performance Anode Material for Sodium-Ion Batteries. *Adv. Energy Mater.* **2014**, *4*, 1301584.
(19) Jache, B.; Adelhelm, P. Use of Graphite as a Highly Reversible Electrode with Superior Cycle Life for Sodium-Ion Batteries by Making Use of Co-Intercalation Phenomena. *Angew. Chem.* **2014**, *126*, 10333−10337.
(20) Kim, H.; Hong, J.; Park, Y.-U.; Kim, J.; Hwang, I.; Kang, K. Sodium Storage Behavior in Natural Graphite using Ether-based Electrolyte Systems. *Adv. Funct. Mater.* **2015**, *25*, 534−541.
(21) Kim, H.; Hong, J.; Yoon, G.; Kim, H.; Park, K.-Y.; Park, M.-S.; Yoon, W.-S.; Kang, K. Sodium intercalation chemistry in graphite. *Energy Environ. Sci.* **2015**, *8*, 2963−2969.
(22) Jung, S. C.; Kang, Y.-J.; Han, Y.-K. Origin of excellent rate and cycle performance of Na^+-solvent cointercalated graphite vs. poor performance of Li^+-solvent case. *Nano Energy* **2017**, *34*, 456−462.
(23) Han, P.-c.; Chung, S.-C.; Lin, S.-k.; Yamada, A. Ab initio study of sodium intercalation into disordered carbon. *J. Mater. Chem. A* **2015**, *3*, 9763−9768.
(24) Wen, Y.; He, K.; Zhu, Y.; Han, F.; Xu, Y.; Matsuda, I.; Ishii, Y.; Cumings, J.; Wang, C. Expanded graphite as superior anode for sodium-ion batteries. *Nat. Commun.* **2014**, *5*, 4033.
(25) Yoo, E.; Kim, J.; Hosono, E.; Zhou, H.-s.; Kudo, T.; Honma, I. Large reversible Li storage of graphene nanosheet families for use in rechargeable lithium ion batteries. *Nano Lett.* **2008**, *8*, 2277−2282.
(26) Pierson, H. *Handbook of Carbon, Graphite, Diamond and Fullerenes*; Noyes Publications: Park Ridge, NJ, 1994.
(27) Vázquez-Santos, M. B.; László, E.; Rouzaud, J.-N.; Martínez-Alonso, A.; Tascón, J. M. D.; Tascón, J. M. Graphitization of highly porous carbons derived from poly(p-phenylene benzobisoxazole). *Carbon* **2012**, *50*, 2929−2940.
(28) Wang, X.; Zhang, G. M.; Zhang, Y. L.; Li, F. Y.; Yu, R. C.; Jin, C. Q.; Zou, G. T. Graphitization of glassy carbon prepared under high temperatures and high pressures. *Carbon* **2003**, *41*, 188−191.
(29) Yoon, S. B.; Chai, G. S.; Kang, S. K.; Yu, J.-S.; Gierszal, K. P. Graphitized Pitch-Based Carbons with Ordered Nanopores Synthesized by Using Colloidal Crystals as Templates. *J. Am. Chem. Soc.* **2005**, *127*, 4188−4189.
(30) Jaroniec, D.; Tarascon, J.-M. Towards greener and more sustainable batteries for electrical energy storage. *Nat. Chem.* **2015**, *7*, 19.
(31) Maldonado-Hódar, F. J.; Moreno-Castilla, C.; Rivera-Utrilla, J.; Hanzawa, Y.; Yamada, Y. Catalytic graphitization of carbon aerogels by transition metals. *Langmuir* **2000**, *16*, 4367−4373.
(32) Ōya, A.; Marsh, H. Phenomena of catalytic graphitization. *J. Mater. Sci.* **1982**, *17*, 309−322.
(33) Sinclair, R.; Itoh, T.; Chin, R. In Situ TEM Studies of Metal-Carbon Reactions. *Microsc. Microanal.* **2002**, *8*, 288−304.
(34) Chen, Y.-Z.; Wang, C.; Wu, Z.-Y.; Xiong, Y.; Xu, Q.; Yu, S.-H.; Jiang, H.-L. From Bimetallic Metal-Organic Framework to Porous Carbon: High Surface Area and Multicomponent Active Dopants for Excellent Electrocatalysis. *Adv. Mater.* **2015**, *27*, 5010−5016.
(35) Qin, J.; Wang, T.; Liu, D.; Liu, E.; Zhao, N.; Shi, C.; He, F.; Ma, L.; He, C. A Top-Down Strategy toward SnSb In-Plane Nanoconfined 3D N-Doped Porous Graphene Composite Microspheres for High Performance Na-Ion Battery Anode. *Adv. Mater.* **2018**, *30*, 1704670.
(36) Sun, Z.; Yan, Z.; Yao, J.; Beitler, E.; Zhu, Y.; Tour, J. M. Growth of graphene from solid carbon sources. *Nature* **2010**, *468*, 549.
(37) Barman, B. K.; Nanda, K. K. Prussian blue as a single precursor for synthesis of Fe/Fe_3C encapsulated N-doped graphitic nanostructures as bi-functional catalysts. *Green Chem.* **2016**, *18*, 427−432.
(38) Hu, J.; Zheng, J.; Tian, L.; Duan, Y.; Lin, L.; Cui, S.; Peng, H.; Liu, T.; Guo, H.; Wang, X.; Pan, F. A core−shell nanohollow-γ-Fe_2O_3@ graphene hybrid prepared through the Kirkendall process as a high performance anode material for lithium ion batteries. *Chem. Commun.* **2015**, *51*, 7855−7858.
(39) Lim, Y. V.; Wang, Y.; Kong, D.; Guo, L.; Wong, J. I.; Ang, L. K.; Yang, H. Y. Cubic-shaped WS_2 nanopetals on a Prussian blue derived nitrogen-doped carbon nanoporous framework for high performance sodium-ion batteries. *J. Mater. Chem. A* **2017**, *5*, 10406−10415.
(40) Wickramaratne, N. P.; Perera, V. S.; Park, B.-W.; Gao, M.; McGimpsey, G. W.; Huang, S. D.; Jaroniec, M. Graphitic mesoporous carbons with embedded prussian blue-derived iron oxide nanoparticles synthesized by soft templating and low-temperature graphitization. *Chem. Mater.* **2013**, *25*, 2803−2811.
(41) Yang, J.; Hu, J.; Weng, M.; Tan, R.; Tian, L.; Yang, J.; Amine, J.; Zheng, J.; Chen, H.; Pan, F. Fe cluster pushing electrons to N-doped graphitic layers with Fe_3C (Fe) hybrid nanostructure to enhance O_2 reduction catalysis of Zn-air batteries. *ACS Appl. Mater. Interfaces* **2017**, *9*, 4587−4596.
(42) Lou, X. W.; Chen, J. S.; Chen, P.; Archer, L. A. One-pot synthesis of carbon-coated SnO_2 nanocolloids with improved reversible lithium storage properties. *Chem. Mater.* **2009**, *21*, 2868−2874.
(43) Gottstein, G. *Physical Foundations of Materials Science*; Springer Science & Business Media, 2013.
(44) Aparicio, C.; Machala, L.; Marusak, Z. Thermal decomposition of Prussian blue under inert atmosphere. *J. Therm. Anal. Calorim.* **2011**, *110*, 661−669.

DOI: 10.1021/acsami.9b07206
ACS Appl. Mater. Interfaces 2019, 11, 24164−24171

(45) Chipman, J. Thermodynamics and phase diagram of the Fe-C system. *Metall. Mater. Trans. B* **1972**, *3*, 55−64.
(46) Li, Z.; Bommier, C.; Chong, Z. S.; Jian, Z.; Surta, T. W.; Wang, X.; Xing, Z.; Neuefeind, J. C.; Stickle, W. F.; Dolgos, M.; Greaney, P. A.; Ji, X. Mechanism of Na-Ion Storage in Hard Carbon Anodes Revealed by Heteroatom Doping. *Adv. Energy Mater.* **2017**, *7*, 1602894.
(47) Li, S.; Qiu, J.; Lai, C.; Ling, M.; Zhao, H.; Zhang, S. Surface capacitive contributions: Towards high rate anode materials for sodium ion batteries. *Nano Energy* **2015**, *12*, 224−230.
(48) Zou, G.; Wang, C.; Hou, H.; Wang, C.; Qiu, X.; Ji, X. Controllable Interlayer Spacing of Sulfur-Doped Graphitic Carbon Nanosheets for Fast Sodium-Ion Batteries. *Small* **2017**, *13*, 1700762.

DOI: 10.1021/acsami.9b07206
ACS Appl. Mater. Interfaces 2019, 11, 24164−24171